Full Paper

NUMERICAL AND EXPERIMENTAL INVESTIGATIONS INTO THE EFFECTS OF COMPLEX GEOMETRY ON THE MECHANICAL PERFORMANCE OF ALUMINUM 6063 ALLOY

B. O. Malomo
Department of Mechanical Engineering, Obafemi Awolowo University, Ile-Ife, Nigeria
bobmalom@oauife.edu.ng

B. Z. Adewole
Department of Mechanical Engineering, Obafemi Awolowo University, Ile-Ife, Nigeria

B. A. Olokuntoye
Department of Mathematics, Obafemi Awolowo University, Ile-Ife, Nigeria

W. A. Tijani
Department of Mechanical Engineering, Obafemi Awolowo University, Ile-Ife, Nigeria

A. T. Alo
Department of Mechanical Engineering, Obafemi Awolowo University, Ile-Ife, Nigeria

H. A. Owolabi
Department of Mechanical Engineering, Obafemi Awolowo University, Ile-Ife, Nigeria

S. A. Adio
Department of Mechanical Engineering, Obafemi Awolowo University, Ile-Ife, Nigeria

ABSTRACT

This study investigates the relationship between variations in the geometric configurations of an aluminum alloy's complex structure and the evolution of its tensile property towards improving its mechanical performance. A prototype aluminum 6063 structure with geometric features of tapered cylinder, convergent cones, cylinder, and stepped cuboids was designed. The heat transfer and solidification analysis were simulated on the structure in the ANSYS software environment to obtain the cooling rates at each of the change of sections. A heat transfer model was used to calibrate the geometric constraints. The experimental validation was performed by sand-casting. The geometric constraints were modeled with variable-sized chills of representative heat transfer coefficients and the temperature-time-history was obtained during casting. Mechanical tests were conducted at the change of sections and the tensile behavior was obtained. The results showed that variability of the heat transfer coefficients corresponds to associated variability in mechanical performance which is in agreement with the simulations. The effect of variations in the cooling rates across the complex geometry suggests that tensile behavior can be closely controlled. Microstructural investigations also confirmed that by controlling temperature gradients, the morphology of the alloy can be tuned for better mechanical performance.

Keywords: solidification, complex geometry, aluminum 6063, ANSYS.

1. INTRODUCTION

A non-uniform geometric structure alters the distribution of mechanical behavior significantly during its forming process. This is critical to the integrity of highly sensitive components in aerospace and automotive engines operating under high temperature loading conditions. Hence, there is now a strong requirement that structures in the aerospace and automotive industries retain their physical characteristics and mechanical integrity for a prolonged period in their entire useful service life (Zhang et al., 2017). This is true especially for certain critical components such as the single-crystal superalloy turbine blades, crankshafts, and aero-engine components in avoiding catastrophic damage while maintaining optimal performance. Most of these components are complex-shaped, and the propensity for incipient failures to initiate at points of discontinuities is usually very high. As a result, to ensure that quality is not compromised, sophisticated and costly processes are usually employed to circumvent the manufacturing difficulties, which, on a large scale, could prove to be prohibitive. Hence, it is of utmost importance, from an economic standpoint, that straight-forward and easy-to-implement procedures are developed. To achieve this, the intricacies of molten metal solidification in complex geometries during casting need to be better understood.

Scientifically, it has been shown that in the solidification of a pure metal, the transformation from the

liquid phase to the solid solution, occurs across a non-equilibrium independent interface where it is impossible to achieve total uniformity of the solid at each temperature during cooling. Consequently, heterogeneities are formed in the chemical composition of the solidifying system (Jarry and Rapphaz, 2018). This ultimately leads to macrosegregation, shrinkage porosity, and other defects that negatively impact the mechanical behavior. Since contraction due to density changes at the liquid-solid interface during solidification is inevitable, the consequent effects of dimensional variation in cooling for the solidifying media can be studied to elicit a set of criteria to control the effects of solidification on mechanical performance. In this perspective, the solidification study of a phase change material (PCM) around a curved cold tube was performed by Ismail *et al.* (2012). In their work, the effects of cooling fluid flow parameters were investigated with respect to the time for complete solidification and the solidified mass. Similarly, Taghilou and Talati (2018), developed an approximate analytical model to evaluate the temperature distribution and position of the solid-liquid interface during the solidification of the PCM to correlate the solidification time with the geometrical features of a two-dimensional finned container. Simmonetti and Fox (2019), developed new experimental methods to encase complex parts in blocks of crystal-clear ice regarding the detection of damage in critical components of complex geometry. Their results indicate that by controlling the propagation of the solidification front while water is freezing, it is possible to prevent the formation of cracks inside the ice volume. Fan *et al.* (2015), investigated the effect of directional solidification parameters on the microstructural characteristics and mechanical properties of Ti-49Al alloy and found a correlation between higher cooling rates and enhanced mechanical performance. Zhang *et al.* (2016), showed how the dendritic morphology could be modified for crystal orientation control in Ti-AlNb alloys through directional solidification.

With respect to aluminum alloys, controlling the grain size is a profound strategy to minimizing the effect of segregation due to the advancement of the solidification front in the melt. Solute segregation is a known phenomenon that deteriorates the mechanical properties. In this purview, the effect of mold filling oscillations in complex geometries have been investigated by Bedel *et al.* (2019) for low pressure castings, and a predictive model was developed to analyze the effect of geometric parameters impacting the oscillations. Tang *et al.* (2019), also implemented a scheme in the solidification of Al-5.0Mg-3.0Zn-1.0Cu where it was discovered that a higher cooling rate helps to increase solute concentrations in promoting the transformation from the GP II zone to η' phase and ultimately enhancing the mechanical behavior. A grain coarsening phenomenon associated with fast cooling rates has been explained by the interdependency theory for grain refinement in relation to both the constitutional undercooling zone ahead of the solid-liquid interface and the growth restriction factor of the solutes (Guofang *et al.*, 2018). Similarly, according to Benjunior *et al.* (2017), a sharp variation in cooling rate has been found to refine the microstructure and improve grain circularity while studying the relationship between solidification rate, metallurgical behavior, and fraction phase growth of wrought aluminum 6061. Also, by controlling pouring temperatures and varying chill sizes to control the cooling rates, a finer grain structure coupled with better mechanical properties had been observed (Wankhede *et al.*, 2018). It is well known that using end chills can promote directional solidification, which accelerates solidification and enhances the mechanical behavior. Based on these concepts, this paper focuses on providing a framework to strategically implement controlled cooling aimed at addressing the variations in mechanical behavior of aluminum alloy castings with complex geometries.

2. NUMERICAL MODELLING

2.1. Theoretical formulation and model description

According to solidification theory, metal casting involves a process of unstable heat conduction at the molten metal-mold cavity interface. For a hypothetical cylindrical mold, a solid layer is assumed to be formed at the cold inner wall with the outer wall being insulated. The solidification front propagates in the outward direction. Hence heat transfer takes place in the radial direction and its effects in the z-direction is neglected (Ismail and Batista de Jesus, 2001). The fluid is incompressible and Newtonian. The heat conduction equation for modelling this problem is given by Equation 1.

$$\frac{1}{r}\left(\frac{\partial}{\partial r}\left(k.r\frac{\partial T}{\partial r}\right)\right)+\frac{1}{r^2}\frac{\partial}{\partial x}\left(\frac{\partial T}{\partial \varphi}\right)=\rho.c.\frac{\partial T}{\partial t} \quad (1)$$

where r, φ are the cylindrical coordinates, x is the longitudinal direction of heat conduction, ρ the density, c, the specific heat, t, the Time, T, the Temperature, and k is the thermal conductivity.

The solid-liquid interface is considered as isothermal occurring at a phase change temperature T_p. Hence the conventional boundary conditions for the solid-liquid interface can be written as:

$$T_{s,l}(r_p,\varphi,t)=T_p \quad (2)$$

The energy balance at the interface that accounts for the latent heat of solidification L can be written in terms of the Stefan condition that must be solved for the solidification front r_p and can be expressed as:

$$\left[1+\left(\frac{\partial r_p}{\partial \varphi}\right)^2\right]\left[k_s\frac{\partial T_s}{\partial r}-\frac{\partial T_l}{\partial r}\right]=\rho L\frac{\partial r_p}{\partial t} \quad (3)$$

where s and l represent the solid and liquid phases respectively.

The prototype geometry of interest is shown in Figure 1. The material is aluminum alloy 6063 with thermo-physical properties and chemical composition as shown on Tables 1 and 2, respectively.

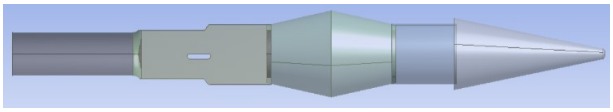

Figure 1: Prototype geometry of cast

Table 1: Thermo-physical properties of aluminum 6063 and air

Material Property	Density (kg/m^3)	Specific heat (J/g^{0}C)	Thermal conductivity (W/m-K)	Liquidus temp. (^{0}C)	Solidus temp. (^{0}C)	Young's modulus (Pa)
AA 6063	2700	0.9	200	620	580	68.9
Air	1.225	1006	0.0242			

Table 2: Chemical composition of aluminum alloy 6063

Alloy	Fe	Mg	Si	Mn	Cr	Cu	Zn	Ti	Al
6063	0.19	0.47	0.54	0.02	0.0007	0.001	0.00033	0.015	Balance

A boundary-value problem was formulated based on Equations (1) to (3) and implemented in finite element model in the ANSYS fluent environment through the standard k-ε turbulence model given by:

$$\frac{\partial}{\partial x_i}(\rho u_i k) = \frac{\partial}{\partial x_i}\left(\frac{\mu_\varepsilon}{\sigma_k}\frac{\partial_k}{\partial x_i}\right) + \mu_t\left(\frac{\partial u_i}{\partial x_j} + \frac{\partial u_j}{\partial x_i}\right)\frac{\partial u_i}{\partial x_j} - \rho\varepsilon \qquad (4)$$

$$\frac{\partial}{\partial x_i}(\rho u_i \varepsilon) = \frac{\partial}{\partial x_i}\left(\frac{\mu_t}{\sigma_\varepsilon}\frac{\partial_\varepsilon}{\partial x_i}\right) + C_{1_\varepsilon}\frac{\varepsilon}{k}u_t\left(\frac{\partial u_i}{\partial x_j} + \frac{\partial u_j}{\partial x_i}\right)\frac{\partial u_j}{\partial x_i} - C_{2_\varepsilon}\rho\frac{\varepsilon^2}{k} \qquad (5)$$

The energy conservation for the fluid

$$\frac{\partial}{\partial x_i}(\rho u_i h) = \frac{\partial}{\partial x_i}(K + K_t)\frac{\partial T}{\partial x_i} \qquad (6)$$

The energy conservation for the die

$$\frac{\partial}{\partial x_i}\left(K_w\frac{\partial T}{\partial x_i}\right) = 0 \qquad (7)$$

2.2. Model constraints

The following assumptions were considered in the simulation process:

i. The liquid phase is a viscous Newtonian fluid, and the flow is assumed to be turbulent with no viscous dissipation.
ii. Thermal energy of the body (mold and cast) is lost by radiation.
iii. Material properties are constant and there is no heat resistance between the phase change material and the mold.
iv. Gas-liquid surface tension effects are negligible.

3. MODEL IMPLEMENTATION

The model shown in Figure 2 is an idealized 2-D analysis of a slice with unit thickness. One-half symmetry is used to reduce the size of the model. Thermal Solid-PLANE35 elements were used to discretize the model. A total of 3556 triangular elements were applied to the structure and metal melt-mold interface (an infinitesimal boundary between the molten metal and the mold). These generated 7346 number of nodes, out of which 1263 nodes belonged to the casting region and 6083 number of nodes belonged to the mold region. The mold is characterized by the properties of sand shown in Table 3 [Narayan et al., 2001].

Convective heat load was applied to the model to initiate the solidification process, at this point, the heat transfer coefficient between sand and mold was specified as 10 W/m-K with the ambient air temperature at 27^{0}C and molten metal at 600^{0}C. A bonded contact condition governs the interface between the cast and the mold sections. By the transient thermal analysis for the model, the boundary conditions indicate the thermal behavior at the sudden contact of molten metal at 973 K with the mold at ambient temperature as convective load is applied. The solution strategy is to choose an automatic time stepping that will account for the modification of temperature variations depending on the severity of nonlinearities in the system. Consequently, the simulation time history was specified between 3.6 and 900 secs (the approximate period for the complete liquid-solid phase transformation at the saturation point when the chills cease to accelerate the removal of heat from the castings, Akhil et al., 2014, and Mehr et al., 2014) respectively.

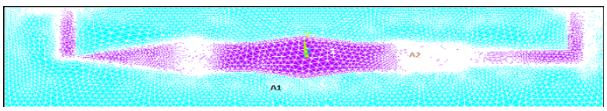

Figure 1: Area plot of the model in ANSYS (A1: mold, A2: cast)

Table 3. Property of sand material

Conductivity (k)	0.519W/m-K
Density	1495kg/m^3
Specific heat (c)	1172.304J/kg.K

3.1. Experimental validation

The complex part simulated was produced by sand casting to implement the results obtained during the heat transfer analysis and solidification process and the properties of the structure were verified by tensile testing. The sand-casting method was chosen based on its low production cost and flexibility to accommodate various complex geometries. A wooden pattern for the casting was fabricated in accordance with the specification shown in Figure 3. The experiments entail, two sets of casts which were divided into the controlled group and the variation group.

The castings were implemented using the wooden pattern as a preform at a pouring temperature of 700^{0}C (Figure 4) with all other factors held constant. The geometry consists of four sections described by *a tapered cylinder, a cylinder, 2 convergent cones and 2 stepped cuboids*. Chills for the adjustment of differential cooling rates were designed for size according to the surface area-volume method and corresponding temperature gradient factor. The chills (Figure 5) were fixed into each section at points T_1, T_2, T_3, T_4 and T_5(Figure 6) prior to casting and K-type thermocouples, connected to a high precision HUATC 12-

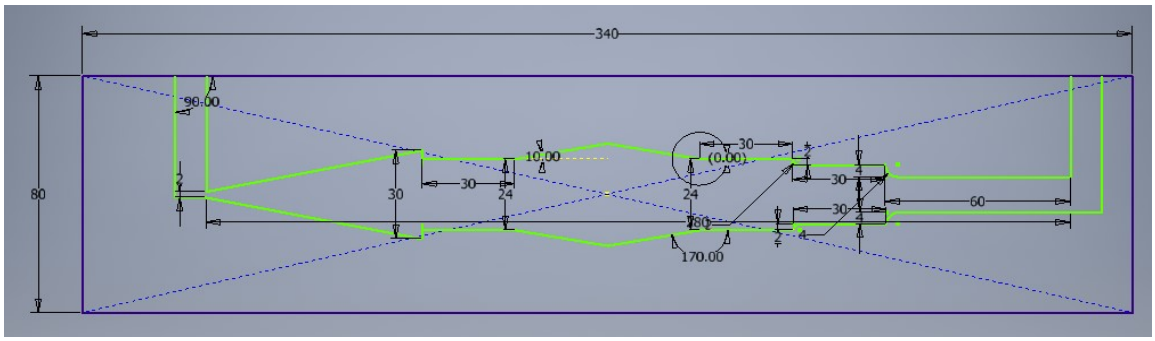

Figure 3: 2D representation of the prototype model (All dimensions in mm)

channel data logger (Figure 7), were subsequently inserted into the mold at each section to measure the temperature variations during solidification. The tip of the geometry was without the attachment of a chill because it was considered as the point of instantaneous freezing.

Figure 4: A wooden pattern

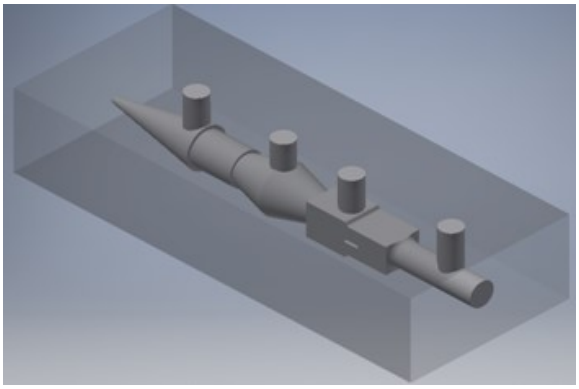

Figure 5: Chills positioning in the cast

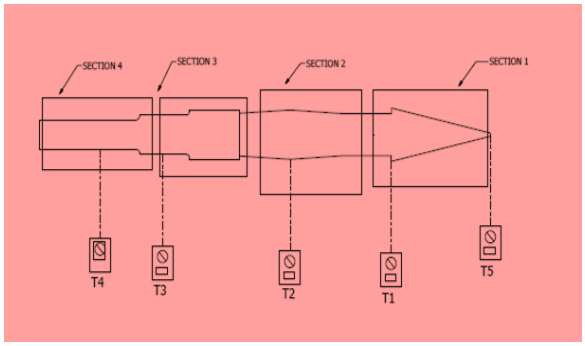

Figure 6: Thermocouple positioning

Figure 7: Data logging process

3.2. Design of gating system

An unpressurized gating system (Figure 8) was designed for the casting process based on the dimensions and geometry (shape factor) of the cast and other parameters, i.e., mass, volume and density. The design consideration includes: Sprue design, Runner design, Gating ratio, Riser design, Ingate design.

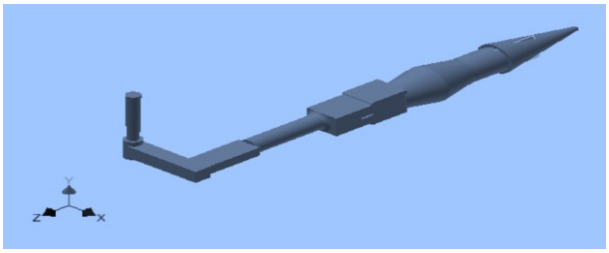

Figure 8: The gating system design

Six sections of the castings were designed as a tapered cylinder, a cylinder, 2 convergent cones and 2 stepped cuboids. Using the weighted surface area-volume method, an approximate volume of each section was calculated as: 9.8cm^3, 9.42 cm^3, 28.27 cm^3, 22.5 cm^3, 12 cm^3 and 10.6 cm^3 respectively.

The specifications for the gating design are shown in Table 4, where, $V_T, L_c, m_t, L_t, L_w, \rho_s$, and ρ_l, are the total cast volume, total cast length, mean thickness of cast sections, largest thickness, largest width of cast sections, density of solid aluminum, density of liquid aluminum, c, is the efficiency factor, and w, is the weight of poured melt respectively.

Table 4: Gating design parameters

V_T,	L_c	m_t	L_t	L_w	ρ_s	ρ_l	c	w
93 cm3	$27cm^3$	$2.07cm$	3cm	3cm	2.7g/cm^3	2.375g/cm^3	0.8	0.5kg

Using these parameters, the shape factor was calculated from:

$$\text{Shape factor} = (L_c + L_w) \div L_t \quad (8)$$

The volume of riser V_R was obtained from the relations $\frac{V_R}{V_T}$,= 0.45

By using the NRL design chart, the riser height and riser diameter for a corresponding V_R, were selected.

The sprue was designed based on the volume of casting required to flow through the system in a six second, interval. The choke area for the sprue was determined by the relations:

$$A_c = w \div (c\rho_l\sqrt{2gH_c}) \quad (9)$$

where, A_c, is the choke area, w, the weight of poured melt, ρ_l, the density of liquid aluminum, g, acceleration due to gravity and H_c, the height of the sprue. The gating ratio of 1:3:3, was selected for the gating system to specify the choke area, runner area and ingate area.

3.3. Mechanical testing

After the casting process, tensile test pieces were machined out of each section of the shape for each group in accordance with ASTM E9-08 specifications using the Instron Universal Test Machine to determine the tensile response of each section.

4. RESULTS AND DISCUSSIONS

4.1. Temperature variations across sections

The simulated temperature response obtained for the controlled and variation groups and are as shown in Figures 9 and 10. The contour plots for the entire simulated surface indicate the evolution of temperatures during solidification of the alloy. The associated cooling curves depicting the thermal performance at the chilled sections are presented in Figures 11 and 12 respectively. The controlled group showed a slight variation in the solidification profile before the freezing point, thus agreeing with Narayan et al. (2001). Hence the transient heat transfer was steady throughout. This phenomenon translates into a faster rate of solute depletion on the cold side of the solid-liquid interface causing predominantly a restricted α-Al phase precipitation. Conversely, for the variation group, the family of curves is characterized by peaks of temperature variations, due to differences in the flux pattern when the solidifying alloy contacts the asperities on the chill surfaces and the mold. At this point, and in-between the peaks the interfacial heat flux continues to vary, giving rise to increased α-Al phase precipitation and progressive nucleation. (Tang et al.,2019).

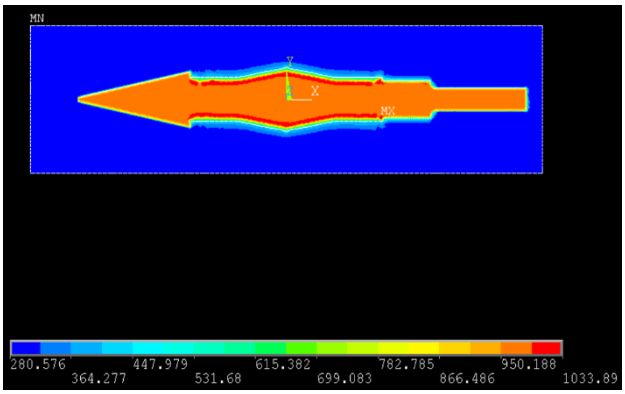

Figure 9: Temperature profile (controlled)

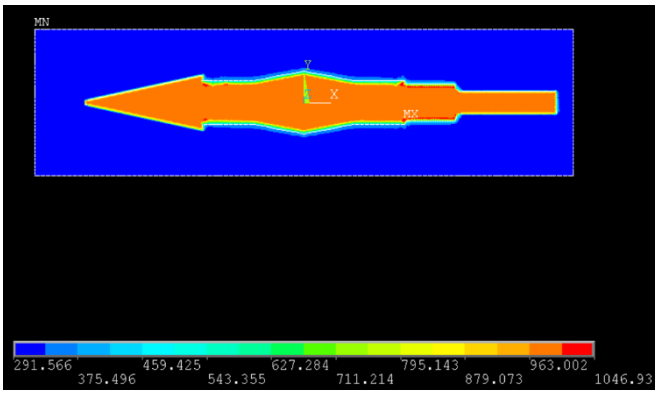

Figure 10: Temperature profile (variation)

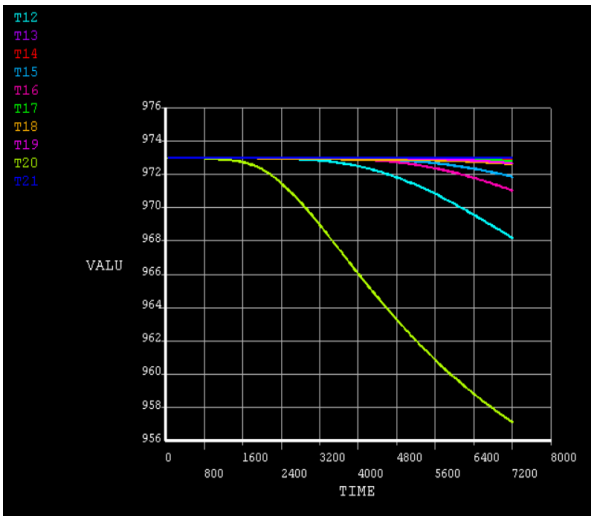

Figure 11: simulated cooling curves (controlled)

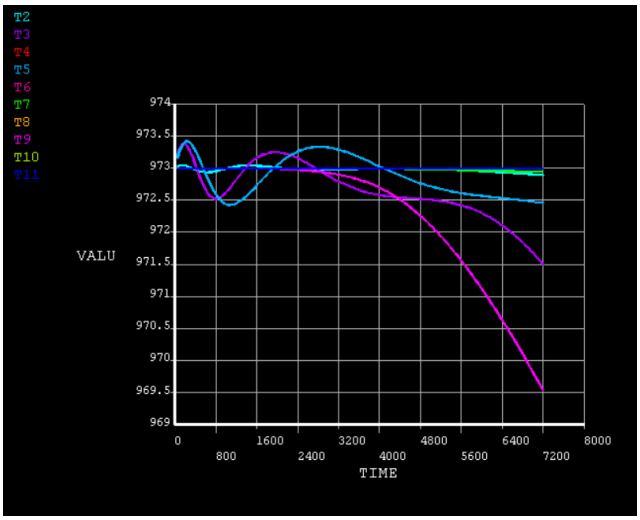

Figure 12: simulated cooling curves (variation)

The heat transfer coefficients for the determination of chill sizes with respect to temperature variations across the mold sections were obtained at the metal-mold interface through an iterative procedure for heat flux variations based on the following relations [Narayan et.al., 2001]:

$$q_r = \frac{\beta(T_c^4 - T_m^4)}{\left(\frac{1}{\alpha_c} + \frac{1}{\alpha_s} - 1\right)} \quad (10)$$

where, q_r is the radiative heat flux at the interface of the sand mold and the casting, β and α_c are the Stephan Boltzmann constants, α_s, the emissivity of the mold surface, T_c and T_m are the surface temperatures of the casting and the mold respectively.

The heat transfer coefficient h is then given by the relations:

$$h = {}^{q_r}/_{T_c - T_m} \quad (11)$$

4.2. Castings

The complex geometries were cast by pouring molten aluminum alloy 6063 from the muffle furnace into the prepared mold pattern. Two sets of castings were made each for the control and variation groups as shown in Figures 13 and 14. The solidification process for the castings took place at ambient conditions.

Figure 13: Control group

Figure 14: Variation group

4.3. Temperature history and cooling curves

The temperature history of each section of the castings obtained through the data logger are presented in Figures 15 and 16 for the control and variation groups respectively. The corresponding cooling curves were obtained by plotting the temperature data against time for each section. It can be readily observed that differential cooling rates occurred across the sections. From Figure 15, it could be observed that an expanded region which describes the transition phase from liquid to solid occurs over a longer interval because a lower latent heat was released during solidification leading to a secondary phase precipitation where the formation of a solid state is evident at the onset of cooling. Conversely, in regard to the solidification behavior of the variation cast group as shown in Figure 16, it was observed that a gradual variation in cooling rates is evident, which is as a result of the controlled application of metal chills of varying heat transfer coefficients in consonance with the variations in geometric profiles. The sudden drop in temperature as shown by the curves indicate that at the onset of cooling, a large amount of latent heat was released in what could be described as a primary phase precipitation. The higher cooling rates in effect promote a large thermal undercooling of the melt, facilitating a higher heterogenous nucleation (Wang et al., 2018).

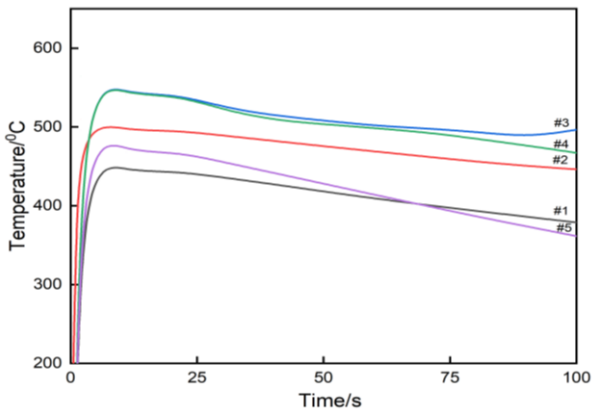

Figure 15: Cooling curves (control group)

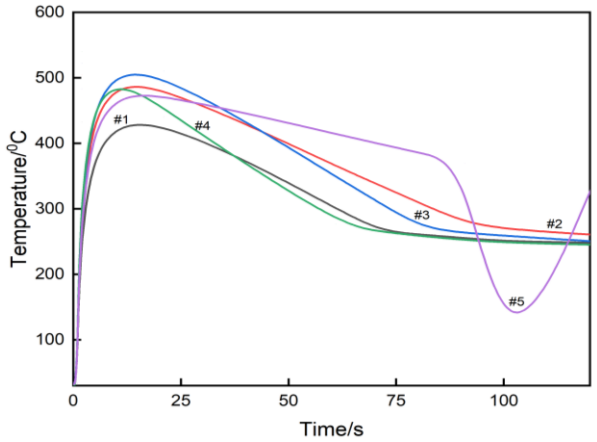

Figure 16: Cooling curves (variation group)

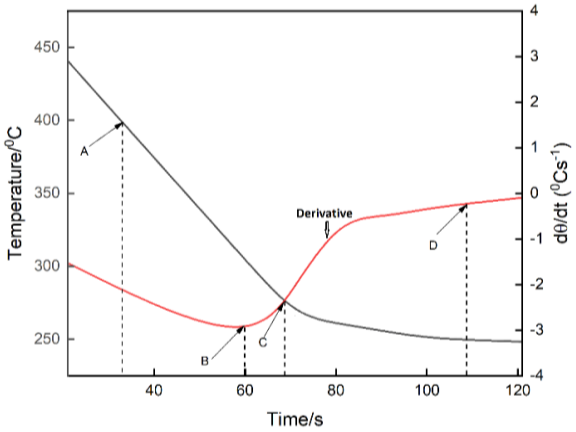

Figure 17: Cooling derivatives (control group)

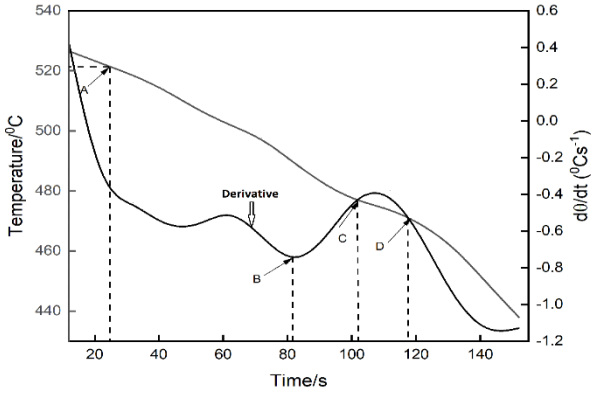

Figure 18: Cooling derivatives (variation group)

4.4. Solidification rate and phase constitutions

Figures 17 and 18 represent the derivative plots of the cooling curves #1 from the control and variation groups, respectively. The cooling rates for the plots were obtained by the linear intercept method. The α-Al phase nucleation occurs at region A as the cooling rate is increased due to the instability of the solid-liquid interface. For the variation group, the nucleation and distribution of aluminum dendrites occurred faster as compared with the control group. The size and distribution of the precipitates determine how the solute concentrations are altered in the aluminum matrix. As higher cooling rates are attained with respect to the variation group, solute concentrations would increase, giving rise to solid solution strengthening (Benjunior et al.,2017). At region A-B, there exists a transition into the binary eutectic Al + Si phase associated with a drop in the cooling rate at point C. The effect of further decline in cooling rate is indicated by the transition points C-D. The formation of various peaks at points C and D suggests the effect of non-equilibrium solidification promotes the formation of ternary and other higher-order eutectic phases in the variation group. On the other hand, a gradual and slower reduction in cooling rates for a longer period suggests that a lower thermal undercooling is in effect for the control group in relation to the variation group. The longer time for solidification facilitates the growth of intermetallics which is justified by the larger size of region C-D in Figure 17. But since, nucleation continues within the constitutional undercooling zone, there is a greater specific dendritic boundary area in the volume which prevents the fast development of intermetallics in the variation group (Feng et al., 2019). At any rate, a homogenous distribution of the intermetallic phases would potentially influence the mechanical performance of the solidified alloy.

4.5. Solidification and mechanical behavior

The tensile plots of the control and variation groups indicating the responses of samples taken from the geometrical sections to peak tensile stresses are shown Figures 19 and 20, respectively. In general, there is an increase in the tensile strengths of the geometrical sections for the variation group relative to the control group.

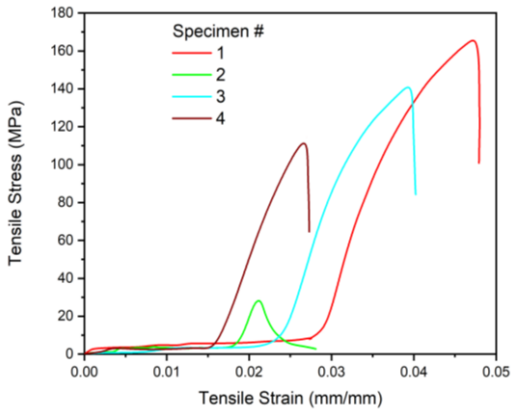

Figure 19: Tensile plot for sections (control)

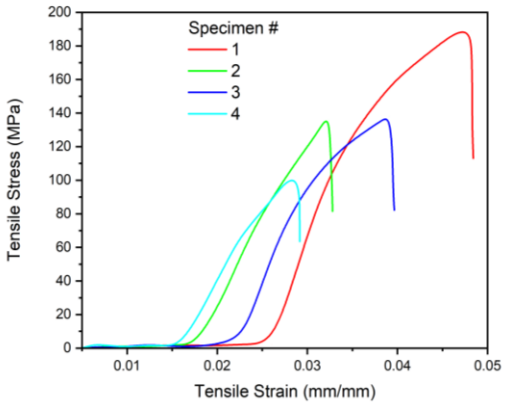

Figure 20: Tensile plot for sections (variation)

It is objective to attribute this to the effect of controlled cooling, because a progressive nucleation within the constitutional undercooling zone due to variations in the cooling rates leads to grain refinement caused by the restriction of the primary grain. However, it is quite interesting to note that the variability in tensile behavior with average cooling rates across the sections is minimal for the variation group. For the control group, the calculated variations are -73%, +369%, and +17.4% for sections #1 (0.57^{0}C)-#2 (0.33^{0}C), #2-#3 (1.68^{0}C) and #3-#4 (2.81^{0}C) respectively. On the other hand, the representations in the variation group were -22.57%, +55.8% and 8.3% for sections #1 (2.71^{0}C)-#2 (1.44^{0}C), #2-#3 (3.69^{0}C) and #3-#4 (3.44^{0}C) respectively. It may be argued that the reason for this occurrence may be attributed to differential cooling rates at the interfaces between the sections which is more prominent between the adjacent sections #1-#2 and #2-#3. A significant drop in cooling rates between these sections could lead to the formation and accumulation of residual intermetallic phases preventing the growth of precipitates. A coarsening effect is also feasible due to recovery to a higher cooling rate, leads to a small undercooling zone which also could impart a detrimental action on the tensile strength due a reduced driving force for nucleation. However, as the cooling rates increase, the solubility of the alloying elements (Si, Mn) in solid solution increases due to the phase-transition effect. When the solubility in the alloy system exceeds the equilibrium state, supersaturated solid solution results, which in turn promotes a variation in the strain field that resists deformation due the interactions between dislocations and the strain field (Chen et al., 2014; Zhang et al., 2018). At lower cooling rates, the alloying elements at the solid-liquid interface diffuse into intermetallics, which in turn is responsible for a decline in mechanical behavior.

4.6. Microstructural characterizations

The microstructures of the control and variation samples at different segments of the solidified alloy investigated by the scanning electron microscopy (SEM) are shown in Figures 21 (a-d) and 22 (a-d) respectively. Generally, the microstructures are composed of primary α-Al and modified eutectic silicon features. A sparse arrangement of dendrites with coarse silicon eutectic phases is noticeable in Figure 21 but a more refined microstructure consisting of higher dendritic densities and an even distribution of microporosities can be observed in Figure 22. This characteristic can be attributed to the enhanced cooling rates effect giving rise to a relative increase in the solid solubility of silicon within the α-Al phase and promoting the formation of lamellar eutectic silicon features (Housseni et al., 2013).

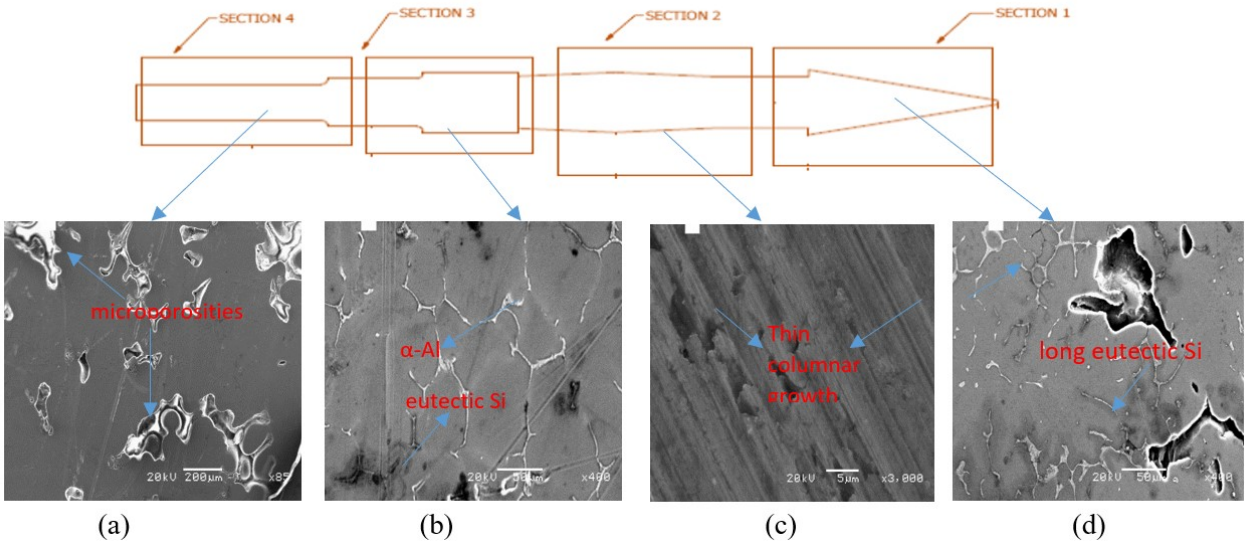

Figure 21: The micrographs of control samples at different geometric sections (a-d)

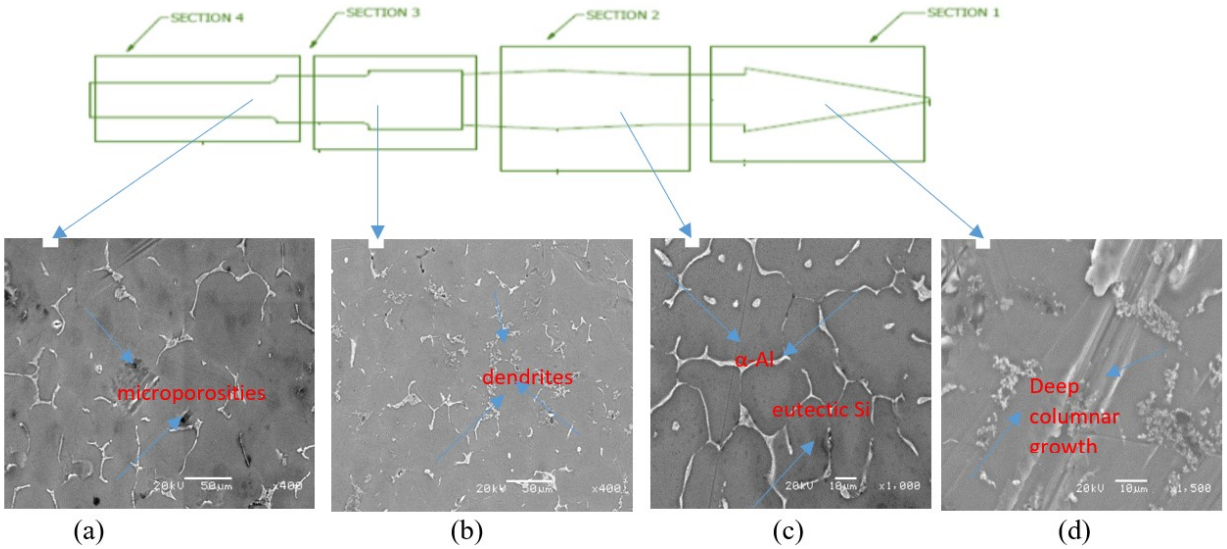

Figure 22: The micrographs of variation samples at different geometric sections (a-d)

With slow cooling it is known that a homogenous composition can be attained at all sections of the molten liquid alloy but conversely, uniformities of the solid cannot be reached, hence heterogeneities are present in the alloy structure. These heterogeneities are the driving potential for micro-segregations (Antonio et al., 2017). During spontaneous cooling, the growth of dendrites is retarded as can be observed in all of the micrographs in Figure 21, because latent heat is absorbed by the effect of temperature gradients giving no room for undercooling of the melt. Therefore, the resulting homogenous growth of nuclei promoted the formation of equiaxic crystals which creates a freezing band that slowed down the growth of dendrites and causing a non-progressive variation in solute distributions along the solidifying mass, leading to the formation of a thinner columnar structure. The drop in mechanical properties may be attributed to the development of the columnar structures which introduced anisotropic properties in the control samples by the planes of structural weakness as the crystals impact on one another, hence, and forthwith making them vulnerable to cracking under tensile deformation. Furthermore, the presence of thinner and longer primary eutectic silicon particles may have induced cracks owing to their supposedly incoherent bonding with the α-Al phase [Zhang et al., 2018].

On the other hand, by controlling the temperature gradients using the chills of varying heat transfer coefficients (Figure 22 (variation samples)), a continuous isothermal heat transfer process is maintained between the mold and the alloy at time $t_1 < t_2 < t_3$. Therefore, since the alloy temperature at the center of the mold would be significantly higher for a longer period of time as compared with that of the spontaneously-cooled alloy, the higher melting temperature translates to the formation of deeper columnar structures which is beneficial to the enhancement of mechanical behavior. This is also because a reduction in the growth of nucleating agents enhanced the solute concentrations in the liquid metal with time, as manifested by the multiplication of the dendrites and the regularity of their configurations, which specifically suggest that accelerated heterogenous nucleation of equiaxic grain was in effect (Zhang et al., 2008). Furthermore, the fast-cooling process introduces a stationary diffusion layer at the solid-liquid interface/interphase where solidification takes place; and by virtue of the differential between the solute concentrations at the liquid and solid regions in relation to the average composition in the alloy, the variation in the microstructures and ultimately the tensile behaviors of the geometric sections is justified. This underscores the fact that by imposing a temperature gradient at the solid-liquid interface of alloys, morphological instabilities can be introduced at migrating solid-liquid interfaces to effectively facilitate dendritic growth, modify eutectic silicon and limit the effects of segregations.

5. CONCLUSIONS

1. The distribution of temperature across a tapered cylinder, two convergent cones, a cylinder and two stepped cuboid sections of a complex geometry casting was performed by numerical simulation and the solidification profile evolved was defined by a criterion for controlled cooling.

2. The cooling curves obtained during the castings indicated that by applying chills of varying sizes in relation to the geometrical asperities, the results of the simulation can be successfully reproduced. The solidification behavior of the variation group suggests that differential cooling rates can accelerate the period of nucleation and primary phase precipitation.

3. The relative sizes of the transition zones indicate that differential cooling for the variation group can facilitate the formation of various peaks that promote the formation of ternary and other higher-order eutectic phases, while the effect of slow cooling for the control group can facilitate the growth and inhomogenous distribution of intermetallics preventing further nucleation of the primary α-phase.

4. Tensile test results confirmed that higher cooling rates could improve mechanical performance considerably. The effect of variations in the cooling rates across the complex geometry suggests that tensile behavior can be closely controlled. The significant variations in tensile strength of the control group may be attributed to the

short period for instabilities at the solid-liquid interface, due to a relatively prolonged cooling period leading to a reduction in solute concentrations.

5. Microstructural observations confirmed that progressive control of temperature gradients introduced morphological instabilities beneficial to enhancing mechanical behavior.

REFERENCES

Akhil, K.T; Arul, S and Sellamuthu, R (2014). The effect of cooling rate, microstructure and mechanical properties of A356 aluminum alloy in casting, Procedia Materials Science, 5, 362-368, Elsevier Science Ltd.

Antonio, J; Elorz, P; Hernandez, M and Gonzalez, L (2017). Solidification and solid state transformations of metals and alloys, Elsevier Inc. 133-136

Bedel, M; Sanitas, A and El Mansori, M (2019). Geometrical effects on filling dynamics in low pressure casting of light alloys, Manufacturing Processes, 45, 194-207, Elsevier Science Ltd.

Benjunior, B; Ahmad, A; Rashidi, M and Reza, M (2017). Effect of different cooling rates condition on the thermal profile and microstructure of aluminum 6061, Procedia, 184, 298-305, Elsevier Science Ltd.

Chen, R; Shi, Y; Xu, Q; and Liu, B (2014). Effect of cooling rate on solidification parameters and microstructure of Al-7Si-0.3Mg-0.15Fe alloy, Trans. Non Ferrous. Met. Soc. China, 24, 1645-1652, Elsevier Science Ltd.

Fan, J; Liu, J; Tian, S; Wu, S; Wang, S; Gao, H; Guo, J; Wang, X; Su, Y and Fu, H (2015). Effect of solidification parameters on microstructural characteristics and mechanical properties of directionally solidified binary Ti-Al alloy, Alloys and Compounds, 650, 8-14, Elsevier Science Ltd.

Feng, S; Li, L; Chan, K; Zhao, L; Pan, S; Wang, L and Liu, R (2019). Tuning deformation behaviour of $Cu_{0.5}$CoNiCrAl high entropy alloy via cooling rate gradient: an atomistic study, Intermetallics, 112, 106553, Elsevier Science Ltd.

Liang, G; Ali, Y; You, G and Zhang, M. (2018). Effect of cooling rate on grain refinement of aluminum alloys, Materialia, 3, 113-121, Elsevier Science Ltd.

Housseni, V. A; Shabestari, S. G and Gholizadeh, R (2013). Study on the effect of cooling rate on the solidification parameters, microstructures and mechanical properties of LM13 alloy using cooling curve thermal analysis technique, Materials & Design 50, 7-14, Elsevier Science Ltd.

Ismail, K. A. R. and Batista de Jesus, A (2001). Parametric study of solidification of PCM around a cylinder for ice bank applications, Int. J. of Refrigeration, 24, 809-822, Elsevier Science Ltd.

Ismail, K. A. R.; Filho, L. M. and Lino, F. A. M (2012). Solidification of PCM around a curved tube, Int. J. of Heat and Mass Transfer, 55, 7-8, 1823-1835, Elsevier Science Ltd.

Jarry, P and Rapphaz, M (2018). Recent advances in the metallurgy of aluminum alloys. Part 1: Solidification and casting, comptes Rendus Physique, 19 (8), 672-687, Elsevier Science Ltd.

Mehr, F.F; Reilly, C ; Cockcroft, S; Maijer, D and MacKay, R (2014). Effect of chill cooling conditions on cooling rate, microstructure and casting/chill interfacial heat transfer coefficient for sand cast A319 alloy, International Journal of Cast Metals Research, Vol. 27, No. 5, Maney & Son Ltd.

Narayan, K ; Prabhu, W and Griffiths, W. D. (2001). Metal/mould interfacial heat transfer during solidification of cast iron in sand moulds, Int. J. of Cast Metals Research, 14:3, 147-155, DOI: 10.1080/13640461.2001.11819433.

Simmonetti, M and Fox, M (2019). Experimental methods for the ultrasonic testing of complex shaped parts encased in ice, NDT & E International, 103, 1-11, Elsevier Science Ltd.

Taghilou, M and Talati, F (2018). Analytical and numerical analysis of PCM solidification inside a rectangular finned container with time-dependent boundary condition, Int. J. of Thermal Sciences, 133, 69-81, Elsevier Science Ltd.

Tang, H; Wang, Q; Lei, C; Ye, B; Wang, K; Jiang, H; Ding, W; Zhang, X; Lin, Z and Zhang, J (2019). Effect of cooling rate on microstructure and mechanical properties of an Al-5.0Mg-3.0Zn-1.0Cu cast alloy, Alloys and Compounds, 801, 596-608, Elsevier Science Ltd.

Wang, L; Bo, L; Wang, Y; Wu, Di; Jia, P; Zuo, M and Zhao, D (2018). Effect of solidification on the core-shell structure of $Al_{60}Bi_{24}Sn_{16}$ monotecnic alloy, Molecular Liquids, 263, 349-356, Elsevier Science Ltd.

Wankhede, D; Narkhede, B; Mahajan, S and Choudhari, C (2018). Influence of pouring temperature and external chills on mechanical properties of aluminum silicon alloy castings, Materialstoday: Proceedings, 5, 9(3), 17627-17635, Elsevier Science Ltd.

Zhang, L. Y.; Jiang, Y. H.; Ma, Z; Shan, S. F.; Jia, Y. Z.; Fan, C. Z. and Wang, W. K. (2008). Effect of cooling rate on solidified microstructure and mechanical properties of aluminum-A356 alloy, Material Processing Technology 207, 107-111, Elsevier Science Ltd.

Zhang, P; Li, Z; Liu, B and Ding, W (2017). Tensile properties and deformation behaviours of a new aluminum alloy for high pressure die casting, Mater. Sci. & Tech, 33(4), 367-378 Elsevier Science Ltd.

Zhang, Q; Xue, H; Tang, Q; Pan, S; Rettenmayr, M and Zhu, M (2018). Microstructural evolution during temperature zone melting: Cellular automaton simulation and experiment, Computational Materials Science, 146, 204-212, Elsevier Science Ltd.